Successive High-Resolution (H$_2$O)$_n$-GCIB and C$_{60}$-SIMS Imaging Integrates Multi-Omics in Different Cell Types in Breast Cancer Tissue

Hua Tian,* Louis J. Sparvero, Tamil Selvan Anthonymuthu, Wan-Yang Sun, Andrew A. Amoscato, Rong-Rong He, Hülya Bayır, Valerian E. Kagan, and Nicholas Winograd

Read Online

ACCESS | Metrics & More | Article Recommendations | SI Supporting Information

ABSTRACT: The temporo-spatial organization of different cells in the tumor microenvironment (TME) is the key to understanding their complex communication networks and the immune landscape that exists within compromised tissues. Multi-omics profiling of single-interacting cells in the native TME is critical for providing further information regarding the reprograming mechanisms leading to immunosuppression and tumor progression. This requires new technologies for biomolecular profiling of phenotypically heterogeneous cells on the same tissue sample. Here, we developed a new methodology for comprehensive lipidomic and metabolomic profiling of individual cells on frozen-hydrated tissue sections using water gas cluster ion beam secondary ion mass spectrometry ((H$_2$O)$_n$-GCIB-SIMS) (at 1.6 µm beam spot size), followed by profiling cell-type specific lanthanide antibodies on the same tissue section using C$_{60}$-SIMS (at 1.1 µm beam spot size). We revealed distinct variations of distribution and intensities of >150 key ions (e.g., lipids and important metabolites) in different types of the TME individual cells, such as actively proliferating tumor cells as well as infiltrating immune cells. The demonstrated feasibility of SIMS imaging to integrate the multi-omics profiling in the same tissue section at the single-cell level will lead to new insights into the role of lipid reprogramming and metabolic response in normal regulation or pathogenic discoordination of cell−cell interactions in a variety of tissue microenvironments.
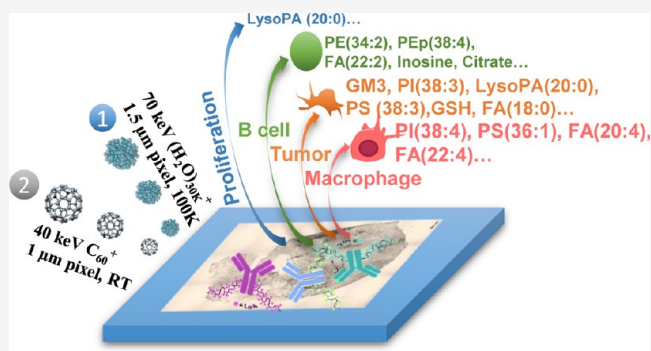
INTRODUCTION

Multi-omics data are essential for understanding the mechanisms underlying normal regulatory processes as well as their disease-specific discoordination. The development of high throughput technologies has advanced cancer research from a single-genomic level to multi-omics approaches, providing an unprecedented view of the complexity of the tumor microenvironment (TME). Combining genomic, epigenomic, and transcriptomic data with proteomic and metabolomic analysis from different cell populations and individual cells has already yielded a new and more complete picture of the complexity and dynamics of the TME.[1−3] This multi-omics information is important for the design of new anti-cancer modalities in the context of precision medicine. However, lipidomic/metabolomic profiling at the single cell level is not yet available, despite the appreciation of the lipid and metabolic reprogramming and signaling that occurs as the early and consequential responses to the dynamic changes in the TME.[4,5] Due to the incompatibility of sample preparation for a lipid/metabolite assay with other omics (e.g., proteomics, transcriptomic, etc.), it is nearly impossible to correlate the different omics profiles within the same sample, let alone their

spatial co-localization at the single cell level. Since changes in metabolites are dynamic and may be transient and short-lived, there is no efficient way to preserve the chemical gradients within single cells. With the increasing interests in the spatial multi-omics, there is an urgent need for new analytical tools and methodologies to characterize the metabolome and its critical component, the lipidome, under minimally disturbed conditions.

Mass spectrometry imaging (MSI) has been adapted for lipid biomarker discovery in various cancers for clinical and research applications due to its unique capability to spatially localize multiple biomolecules in situ, providing chemical distinction within intra-tumor, tumor margin, and healthy tissue for new insights into the disease mechanism and
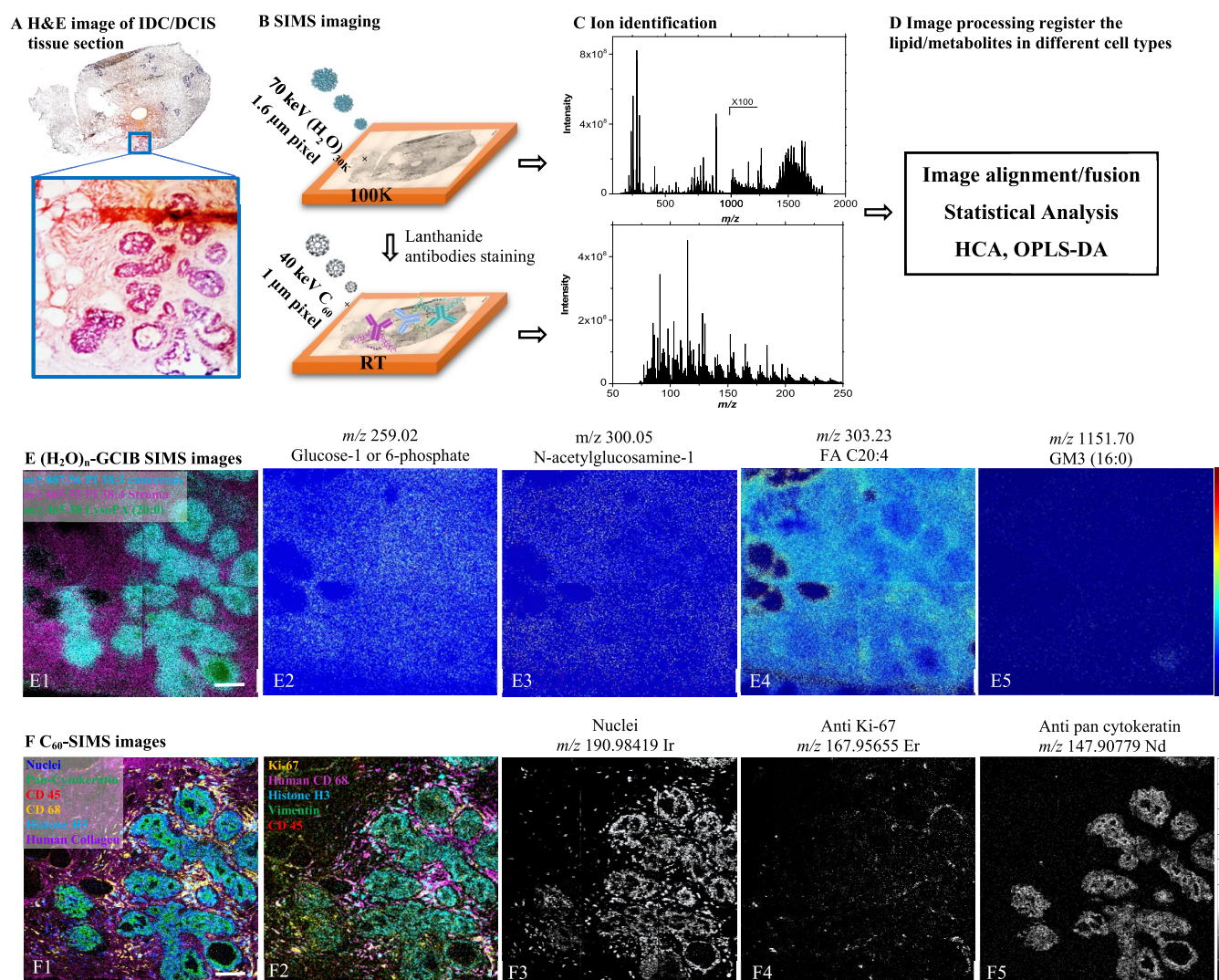
Figure 1. Schematic of the workflow on cell-type specific profiling of multi-omics on the IDC/DCIS tissue section at the single-cell level and select overlay and single-ion images using $(H_2O)_n$-GCIB SIMS and C_{60}-SIMS. (A) H&E staining image of a semi-serial section of IDC/DCIS tissue. The zoom-in image from the region of interest highlighted in blue shows the tumor region in purple and stroma region in pink. (B) SIMS imaging on another fresh-frozen tissue section. First, the cryogenic analysis at 100 K was performed on frozen-hydrated tissue section for molecular imaging (e.g., lipids and metabolites) using $(H_2O)_n$-GCIB-SIMS at a beam spot size of 1.6 μm. This was followed by immunostaining of multiple lanthanide-tagged antibodies on the same frozen tissue section for simultaneous imaging of cell-specific markers using C_{60}-SIMS at a beam spot size of 1.0 μm. (C) Species annotation. The $(H_2O)_n$-GCIB generates intact molecular ions up to m/z 2000 with over 160 identified metabolites and lipids with mass accuracy <50 ppm (Table S2). All the lanthanide antibodies are identified by stable isotopic metal ions. (D) Image alignment and cell segmentation were then conducted to integrate the different omics (metabolites, lipids, and proteins) into different cell types at the single-cell level. (E) Selected $(H_2O)_n$-GCIB-SIMS images of IDC/DCIS tissue from the area highlighted in blue in (A). (E1) Color overlay in the SIMS image of the area highlighted in blue in (A). PI 38:4 at m/z 885.55 in magenta is mainly distributed in the stromal area. PI 38:3 at m/z 887.56 in cyan is representative of the IDC/DCIS region. LysoPA (20:0) at m/z 465.30 in green is located inside the duct, likely indicating an inflammatory response. (E2−E5) Selected single-ion SIMS images of DCIS/IDC tissue. More images are shown in Figure S5. (F) C_{60}-SIMS images of the same tissue post-staining with lanthanide-tagged antibodies and $(H_2O)_n$ GCIB-SIMS profiling. (F1−F2), Color overlay images of various antibody makers. These images show the cell heterogeneity in the TME and precisely localize and correlate different cell types. (F3−F5) Single-ion images for lanthanide-tagged antibodies/markers targeting: nuclei in (F3), Ki-67 for cell proliferation in (F4), and pan-cytokeratin for the epithelial tumor in (F5). More images are shown in Supporting Information Figure S6.

guidance for surgical excision.[6,7] MSI instruments utilizing matrix-assisted laser desorption/ionization,[8] desorption electrospray ionization,[9,10] and liquid extraction surface analysis[11] can obtain proteomic, lipidomic, and metabolomic information, usually with spatial resolutions ranging from several to hundreds of microns. Moreover, these techniques usually require matrix application or drying of the sample, which could cause the delocalization of the biomolecules, particularly for metabolites. Secondary ion mass spectrometry (SIMS) is also

utilized for MSI, and it is coupled with a primary ion beam which offers unprecedented spatial resolution from a few microns down to the submicron level, revealing a more detailed landscape of the lipids and metabolites in healthy/neoplastic tissue. A handful of applications of SIMS on breast cancer tissue have been reported.[4,12]

Although MSI has generated more detailed chemical maps of cancer tissue, there is still a dearth of information on the immune-landscape, phenotype, cell classification, and hetero-

geneity at the single cell level. Several groups tackled this issue by integrating MSI with immunofluorescence imaging,[13,14] conventional histology,[15] and machine learning. Multiplexed ion-beam imaging SIMS has also been established to improve conventional histological approaches. It involves linking distinct lanthanide nuclides to different antibodies for application to formalin-fixed paraffin-embedded (FFPE) tissue followed by SIMS imaging of the lanthanides. This simultaneously maps many cellular epitopes at sub-cellular resolution.[16,17] However, other omics information cannot easily be recovered from the FFPE tissue. The same disadvantage is also associated with other microscopy imaging techniques, such as co-detection by indexing for multiple protein imaging (CODEX), cryogenic electron microscopy, and so forth.[18−20] Thus, the correlation of multi-omics profiling with cell type information for a comprehensive understanding of the TME remains a great challenge for all imaging techniques.

Here, we present a new protocol using sequential $(H_2O)_n$-GCIB and C_{60}-SIMS imaging facilitated by lanthanide-tagged antibodies that identifies lipids and metabolites in different cell types in frozen-hydrated breast cancer tissue. Using the multimodal SIMS imaging, over 100 key lipid and metabolite species are spatially resolved in the TME and correlated with individual cells expressing specific protein markers of cell types/pathways (e.g., tumor epithelial cell, macrophages, immune cells, cell proliferation, etc.). The heterogeneity of the immune landscape and key biomolecules are visualized in the same sample at the single cell level, correlating different omics for the understanding of cell−cell interaction, metabolic regulation during immune response, and phenotype. To our knowledge, this approach is the first attempt to correlate different cell types, as reported by lanthanide-tagged antibodies, with their metabolic and lipidomic status.

■ SUMMARY OF MATERIALS AND METHODS

Two snap-frozen human breast cancer tissue samples [invasive ductal carcinoma/ductal carcinoma in situ (IDC/DCIS) and IDC] were generously provided by Penn State Institute for Personalized Medicine Biobank. Sections of each sample were applied to gold plates and plunge-frozen in liquid N_2 (for SIMS) with additional semi-serial sections for microscopy. An area of DCIS was identified from the IDC/DCIS sample (blue box, Figure 1A) to guide subsequent SIMS on a frozen-hydrated semi-serial section (workflow, Figure 1B−D). Cryogenic $(H_2O)_n$-GCIB-SIMS (for lipids and metabolites) followed by treatment with lanthanide-tagged antibodies (Table S1) and C_{60} SIMS (for cell markers) was performed on a buncher-ToF J105 3D Chemical Imager (Ionoptika, Southampton, UK).[21,22] $(H_2O)_n$-GCIB-SIMS used a 70 keV $(H_2O)_{30k}{}^+$ (1 pA) beam with a beam focused to a subcellular level (refer to Supporting Information Figure S1 for beam focus). The acquisition was 512 × 512 pixels in negative ion mode performed over 840 × 840 μm^2 (1.6 μm per pixel) and 512 × 512 μm^2 (1.0 μm per pixel) for IDC/DCIS and IDC tissue sections, respectively. 40 keV $C_{60}{}^+$ SIMS (5 pA) with positive ion mode acquisition was performed roughly on the areas analyzed by $(H_2O)_n$-GCIB, a 768 × 768 μm^2 location using 768 × 768 pixels on the IDC/DCIS section and a 512 × 512 μm^2 location with 512 × 512 pixels on the IDC section (each 1.0 μm per pixel). Ions of lipids and metabolites were identified by their exact mass assisted by literature reports (Table S2). GCIB and C_{60} images were aligned using in-house

Python code with Hierarchical Cluster Analysis (HCA) and OPLS-DA using custom Python and Cell Profiler 3.0 pipelines,[23] respectively. Refer to the data availability section for the scripts and the Supporting Information for the expanded Materials and Methods.

■ RESULTS AND DISCUSSION

Multimodal Imaging Workflow for Cell-Specific Profiling of Omics. As the integration of multiple omics information at the single-cell level and within the same cell remains a great challenge, a new workflow is adapted using multimodal imaging coupled with computational image processing, as demonstrated on IDC/DCIS tissue in Figure 1. H&E imaging of a serial section is used to annotate cancerous regions (Figure 1A, zoom-in area). On a fresh frozen semi-serial section, cryogenic $(H_2O)_n$-GCIB-SIMS (100 K) is conducted on the annotated region to localize the lipids/metabolites at 1.6 μm beam spot size. This was followed by staining with lanthanide-tagged antibodies on the same frozen-hydrated tissue and imaging of the same region using C_{60}-SIMS (RT) at 1.1 μm beam spot size (Figure 1B). Multi-omics integration in single cells has several advantages: (1) SIMS imaging using two beams takes the advantage of diverse beam properties, $(H_2O)_n$-GCIB-SIMS minimizes in-source fragmentation for the detection of intact biomolecules (e.g., lipids and metabolites), while C_{60} is more energetic for the detection of the lanthanide reporters for each antibody.[24] (2) Frozen-hydration preserves chemical gradients at a near-natural state during analysis, especially for metabolites that are in dynamic flux and difficult to analyze in single cells. (3) Antibody application on fresh frozen tissue reduces sample manipulation and does not require antigen retrieval as for FFPE tissue. (4) An estimated 300 nm of surface material is removed by image acquisition using the $(H_2O)_n$-GCIB,[25] allowing sequential imaging by C_{60}-SIMS for protein profiling within the same cells on the tissue. The antibody panel (Table S1) is well-studied and targets proliferation and markers of epithelial, mesenchymal, and immune cells, and extracellular matrix.[16,17] The data processing is then performed by annotation of biomolecules/metal ions, image alignment, cell segmentation, and statistical analysis to register the biomolecules to different cell types (Figure 1C,D). We present analysis of an IDC/DCIS tissue section as a model system. The same workflow performed on an IDC tissue is presented in Supporting Information Table S2, Figures S6, S8, and S10.

$(H_2O)_n$-GCIB-SIMS Reveals Molecular Heterogeneity in the TME. Imaging using $(H_2O)_n$-GCIB-SIMS allowed 163 ion species up to m/z 2000 to be selected and partially identified on IDC/DCIS tissue, as shown in Table S2. Imaging at 1.6 μm pixel size elucidates distinct ion distribution patterns corresponding to the anatomical features of cancerous and non-cancerous areas on the H&E image in Figure 1A (blue box inset). Due to the distance between the semi-serial sections, the features highlighted in the inset box of Figure 1 are not perfectly identical with the SIMS images that follow, but rather the H&E image was used as a general reference to aid in selecting an area for SIMS analysis. In the three-channel ion image (Figure 1E1), the m/z 887.56 ion displayed in cyan is assigned to phosphatidylinositol (PI 38:3) and it shows a higher relative intensity in the cancerous cell regions, similar to the purple-stained ductal regions in the H&E image. PI(38:4) at m/z 885.55 in magenta (Figure 1E1) is mainly localized outside of these cancerous regions in the tissue stroma, while
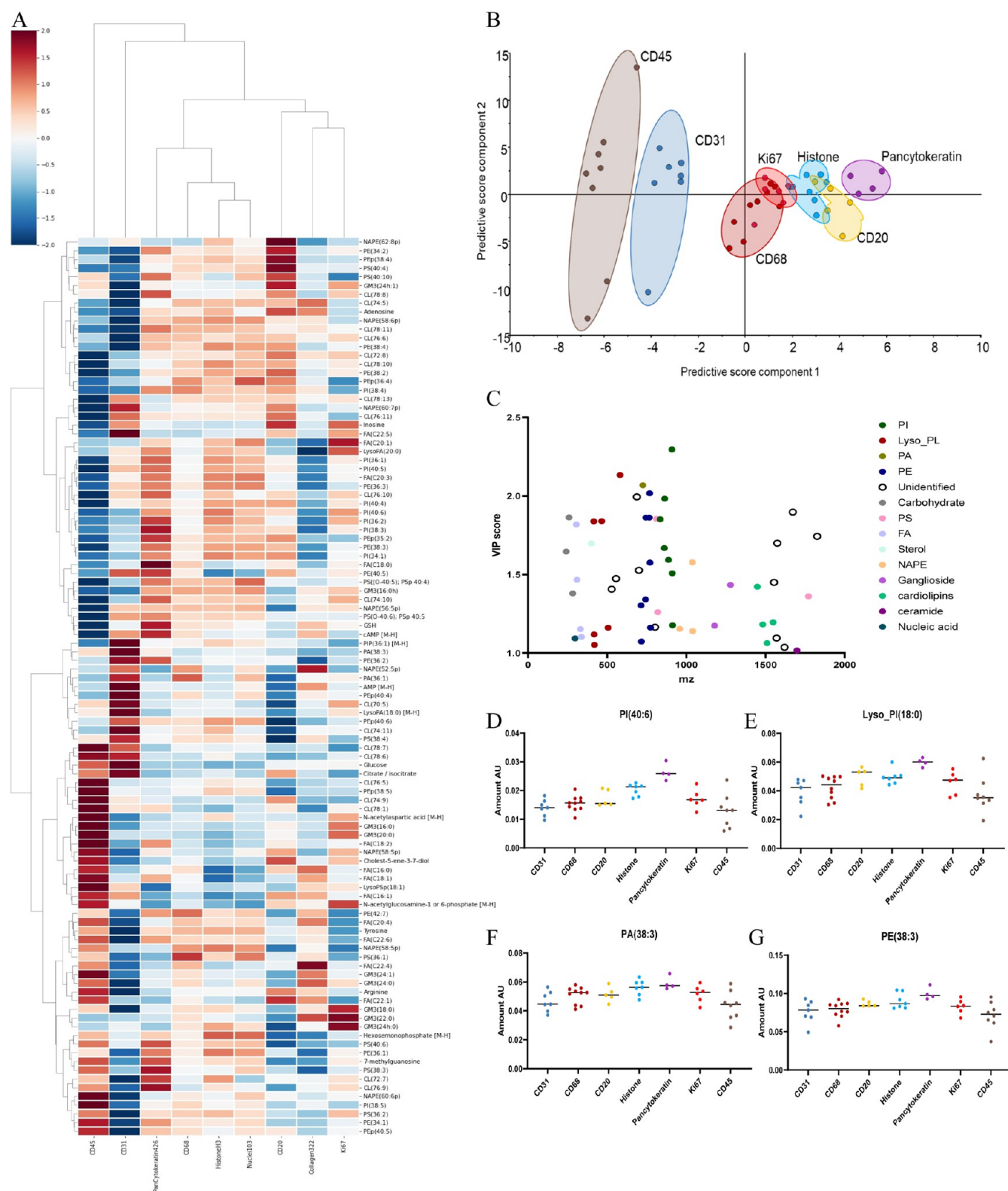
Figure 2. HCA dendrogram and OPLS-DA analysis on IDC/DCIS tissue. (A) HCA showing variation of 103 identified $(H_2O)_n$-GCIB ions (as detailed in Table S2) in the regions, where the nine C_{60}-SIMS cell markers were located. Intensity scale bar indicates $(H_2O)_n$-GCIB ions that are stronger (red) or weaker (blue) by standard deviations above or below their mean intensity, respectively, in areas that overlap with a given cell marker. Identified ions are labeled by assignment and experimental m/z. Hierarchy of clusters are indicated both for cell markers (vertical) and lipids and metabolites (horizontal). (B) OPLS-DA score plot of the metabolome/lipidome associated with each marker. (C) Dot plot showing variable importance for prediction (VIP) score vs m/z of metabolites and lipids. Only significant metabolites and lipids are shown. (D−G) Distribution of the top four species responsible for class separation in OPLS-DA.

lysophosphatidic acid (LysoPA 20:0) at m/z 465.30 in green (Figure 1E1) resides inside the ducts.

The single ion maps of various species up to m/z 2000 are shown in Figures 1E2−E5 and S5. Several metabolic markers for healthy and IDC tissues are mapped as deprotonated molecular ions, such as glucose (Figure S5B1), glucose-1- or 6-phosphate (Figure 1E2) and N-acylglucosamine-1 (Figure 1E3).[26] The dehydrated form of glucose phosphate (Figure S5B2) and adenosine monophosphate (AMP) (Figure S5B4) are observed. However, these could also be formed from in-source fragmentation from the $(H_2O)_n$-GCIB (Figure S2), and also AMP is isomeric to hydroxy GMP [both $C_{10}H_{13}N_5O_7P$ as $(M−H)^-$]. Glutathione (GSH), uridine monophosphate, N-acetylglucosamine-1-phosphate, and cholest-5-ene-3-7-diol are also observed (Figure S5B5,B7−B9, respectively). Notably, glucose monophosphate (Figure 1E2) exhibits only a slight elevation in the cancerous region [compare with PI(38:3), Figure 1E1]. N-acetylglucosamine-1-phosphate (Figure 1E3), which is a metabolic cancer marker, has an unexpectedly elevated distribution outside of the cancerous region.[27]

Various fatty acids, either in free-form or generated as in-source fragments from a precursor lipid ion, are more intense in different regions of the tissue. For example, fatty acid (FA) C18:2, C18:0, C20:3, and C26:2 (Figure S5B10, B11, B13, and B16, respectively) are more intense in the cancerous region, while C20:4 (Figure S5B12) and C22:4 (Figure S5B15) are less intense in those regions. The lack of the highly unsaturated fatty acids C20:4 and C22:4 is possibly associated with the survival mechanism of the cancer cells. Fatty acids with a higher degree of unsaturation are prone to enzymatic and non-enzymatic peroxidation associated with the execution of the regulated cell death programs, particularly ferroptosis and creation of necro-inflammatory foci.[28,29] However, docosahexaenoic acid (DHA C22:6) (Figure S5B14) shows a slightly higher intensity within the cancer cells, which is likely for a higher rate of cellular proliferation and glycopeptidolipid synthesis. Interestingly, anti-inflammatory lipid mediators, particularly some resolvins, have been associated with antitumor activity;[30] however, their intracellular localization within the TME has not been established previously.[4]

Several glycerophospholipid and glycolipid species show very distinct distributions in the tissue. LysoPA(20:0), phosphatidylethanolamine plasmalogen (PEp 34:2), and monosialodihexosylganglioside (GM3 16:0) (Figure S5B17,B19, and B33, respectively) are more intense within the ductal cancerous regions, and possibly involved in or as a result of an inflammatory response. Phosphatidic acid (PA 36:1), phosphatidylserine (PS 36:1), and PI(38:4) (Figures S5B21,B22 and 1E1, respectively) show a higher concentration outside of the cancerous region. Different lipids with less unsaturation, phosphatidylethanolamine PE (36:2), PE(36:1), PE(38:3), PI(34:1), PI(36:2), PI(36:1), PI(38:3), and PI(40:6) (Figure S5B24−B31) are present at a higher relative intensity in the cancerous regions. Interestingly, PI(38:4) (purple in Figure 1 panel E1), previously considered to be upregulated in cancer, is actually more intense in the tissue stroma outside of the cancerous region.

High-Resolution C_{60}-SIMS Imaging (1.0 μm) Reveals Cell Heterogeneity. Roughly, the same region probed by the $(H_2O)_n$-GCIB (Figure 1A) was analyzed after antibody staining as in Figure 1F1,F2 for the color overlay images of different tags and in Figures 1F3−F5 and S7 for single-tag images. These images demonstrate single-cell resolution using

a finely focused C_{60} beam for SIMS imaging. Figure 1F1 clearly outlines the cancerous region by the highly packed nuclei in blue and perinuclear space by anti-pan-cytokeratin in green. Macrophages, labeled by anti-human CD68 (yellow, Figure 1F1), are localized around the ducts and the cancerous cells. Pan-immune cells mapped by anti-human CD45 (red, Figure 1F1) are very sparse in the cancerous region. Chromatin, identified by anti-histone H3 (cyan, Figure 1F1), has some overlap with macrophages but is further away from the cancerous cells, possibly associated with the overall hypo-acetylation of histones during tissue progression from normal to DCIS to IDC.[17] Anti-human collagen I (purple, Figure 1F1) is used to visualize the connective tissue structure. Figure 1F2 also shows the highly proliferative cells by anti-Ki-67 (yellow), which surrounds the cancerous cell core and mesenchymal cells labeled by anti-vimentin (Green).

Molecular Mapping of Lipids and Metabolites in Different Cell Types Demonstrates Cellular Heterogeneity in the Tumor Microenvironment. Co-registration was then performed with the $(H_2O)_n$-GCIB and C_{60}-SIMS images of IDC/DCIS for annotated lipidomic/metabolic profiling to different cell types, as demonstrated in Figure S1. HCA analysis determined considerable similarities between lipid and metabolite expression in the chromatin (histone H3), nuclear (DNA marker), and intracellular epithelial tumor (pan-cytokeratin) regions (Figure 2). Many species that are strong in those three intracellular regions are weak in the extracellular (collagen type I) region and vice versa. For example, various PI speices such as PI 40:6, 38:3, 36:1, 34:1 are strong in the nuclei/chromatin (histone H3)/epithelial tumor (pan-cytokeratin) region but weaker in collagen (Figure 2A). Ki-67 is strongly associated with cell proliferation, and LysoPA(20:0) is more intense in the Ki-67 regions, likely due to its role in cell proliferation.[31,32] Other metabolites that are more intense in the Ki-67/chromatin (histone H3) regions are N-acetylaspartic acid (m/z 174.04) and 7-methylguanosine (m/z 297.10) (Figure 2). These metabolites have been associated with various types of cancers, including breast cancer, and have a prominent role in promoting tumor growth.[27,33] Eight different GM3 species correlated with the Ki-67 regions (Figure 2). Gangliosides have only a limited expression in healthy breast tissue but have been shown to be present in several types of cancers, including IDC.[34−36] Gangliosides are involved in cell adhesion, signal transduction, recognition processes, and proliferation;[37] therefore, our results might be indicative of the neoplastic transformation of breast tissue. GM3 with 22:0, 24:1, and 24:0 ceramides is also elevated in the macrophage (CD68) regions (Figure 2). These might be either associated with the tumor infiltrating macrophages or have been shed by the tumor cells themselves. The latter has been shown to effectively modulate macrophage phenotypes, consequently enhancing angiogenesis in the TME.[38] Elevated levels of saturated and lower levels of unsaturated fatty acids are present in the epithelial tumor (pan-cytokeratin) and Ki-67 regions (Figure 2). This has not been previously documented by liquid chromatography−mass spectrometry[27] because of the lack of spatial information and may be related to the lower sensitivity of the cancer cells to lipid oxidation. In contrast, the CD68-positive macrophages are enriched in highly oxidizable polyunsaturated lipids (Figure 2), some of which may be used as precursors of lipid signals, possibly acting as tumor suppressors.[39,40]

Table 1. Major Differential Lipids and Metabolites between Individual Cell Marker Types[a]

	CD31	CD68	CD20	histone	pancytoleratin	Ki67
CD68	NAPE(58:5p)					
	CL 72:8					
	CL 76:11					
	citrate/isocitrate					
	GM3(16:0h)					
CD20	NAPE(58:5p)	LysoPA(16:0) [M−H$_2$O−M]				
	CL 76:11	GM3(24h:0)				
	CL 78:13	PEp 40:6				
	hexose	PE 36:3				
	arginine	LysoPA 18:1 [M−H$_2$O−M]				
histone	CL 72:8	PE 36:3	PE 36:3			
	NAPE(58:5p)	PI 40:6	GM3(24h:0)			
	PI 40:6	GM3(24:0)	FA_C22:5			
	hexose monophosphate [M−H]	citrate/isocitrate	citrate/isocitrate			
	PA(38:3)	LysoPSp 18:1	NAPE(52:5p)			
	PI 40:6	PS 38:4	PI 34:1	PE 34:1		
pancytoleratin	CL 72:8	LysoPA(16:0) [M−H$_2$O−M]	PI 36:1	PS 38:4		
	hexose monophosphate [M−H]	PI 40:6	PI 40:6	PI 40:6		
	NAPE(58:5p)	PI 36:2	PS 38:4	LysoPI 18:0 [M−H$_2$O−M]		
	PI 36:1	PE 36:3	NAPE(52:5p)	PI 34:1		
Ki67	NAPE(58:5p)	CL 74:10	CL 74:10	LysoPSp 18:1	PI 36:2	
	CL 72:8	CL 78:13	LysoPSp 18:1	PI 36:1	PI 36:1	
	CL 78:13	LysoPA 18:1 [M−H$_2$O−M]	FA_C22:1	NAPE(58:6p)	PS 38:4	
	CL 74:10	CL 78:7	CL 78:1	FA_C22:1	FA_C22:1	
	PE 38:4	NAPE(58:5p)	PI 36:1	PI 36:2	PI 34:1	
CD45	CL 74:5	CL 76:5	CL 76:5	CL 76:5	PI 40:6	CL 74:5
	CL 76:5	CL 74:5	CL 74:5	CL 74:5	CL 74:5	CL 76:5
	arginine	arginine	PE 38:3	PI 40:6	FA_C20:3	PE 38:4
	NAPE(56:5p)	NAPE(56:5p)	PE 38:4	FA_C20:3	CL 76:5	PEp 40:5
	GM3(16:0h)	PE 42:7	hex(3)-hexNAc(3)-cer 44:1	GM3(16:0h)	LysoPI 18:0 [M−H$_2$O−M]	PEp 38:4

[a]Matrix showing the top five known species that showed differences between two markers. Top species were identified using the VIP score from OPLS-DA analysis.

Almost all the assigned PEs are abundant in the nuclei/chromatin (histone H3)/epithelial tumor (pan-cytokeratin) regions (Figure 2), with the exception of PE(40:5) at m/z 792.54 which is high in the epithelial tumor (pan-cytokeratin) region but low in chromatin (histone H3) and nuclei regions. The signal from PE(40:5) is strong in endothelial cells (CD31) along with PE(36:3) at m/z 740.52 and PE(36:2) at m/z 742.53; the other PEs are low in endothelial cells (CD31).

Three different PI species with 38 fatty acyl carbons are identified (PI 38:3, 38:4, and 38:5), all exhibiting very different expression patterns, even though their only structural difference is the degree of unsaturation (Figure 2). PI species are the strongest in the nuclei/chromatin (histone H3)/epithelial tumor (pan-cytokeratin) regions except for PI(38:5) at m/z 883.53 which is higher in the macrophage (CD68) region. All the identified PI species including PI(38:3) at m/z 887.56 are weaker in the collagen region except for PI(38:4) at m/z 885.54 and PI(38:5) which had moderate intensities. PI(38:5) and PI(38:4) are low in the Ki-67 regions, while PI(38:3) is moderate. In contrast, other PI species such as PI(36:2) at m/z 861.55 and PI(40:6) at m/z 909.55 are high in the cell-proliferating (Ki-67) region. Interestingly, PI-3-K/AKT signaling can be activated by estrogen (ER), progesterone (PR), and HER2 thereby regulating the breast cancer cell signaling network. On the other hand, PI-3-K has also been associated with a mechanism of immune resistance in breast cancer,[27] and over-expression of the p110β isoform of PI-3-K has been shown to inhibit the motility of breast cancer cells.[41,42]

PS is normally not found on cell surfaces except as "eat me" signals,[43] and these signals are generally high in the intracellular nuclei/chromatin (histone H3)/epithelial tumor (pan-cytokeratin) regions and lower in the extracellular collagen region (Figure 2). Exceptions include PS(38:4) at m/z 810.53, which is at a similar moderate intensity in all four regions, PS(36:2) at m/z 786.53 which is high in the cell-proliferating (Ki-67) region, and PS(38:4) at m/z 810.53, which is high in the endothelial cells (CD31). Many PS species displayed moderate intensities in the macrophage (CD68) region, in contrast to PS(36:1) at m/z 778.57 which exhibited a stronger signal in that region.

Specific Lipidomic Features of Different Cell Types Present in the TME. HCA by itself is still limited in that it

does not reveal which specific molecular species contribute the most to the distinguishing cell types. Therefore, we further employed OPLS-DA multivariate analysis in combination with single-cell segmentation. The OPLS-DA score plot indicated distinct differences associated with each of the cell markers (Figure 2). Pan-immune (CD45), endothelial (CD31), and epithelial tumor (pan-cytokeratin) cells are well-separated in the plot. Macrophage (CD68) and proliferating cells (Ki-67) overlapped significantly, indicating some metabolic similarities. The top four identified lipid species differentiating each of the cell types are PI(40:6), LysoPI(18:0), PA(38:3), and PE(38:3) (Figure 2).

OPLS-DA analysis is also used to compare lipid/metabolite profiles associated with one cell type versus all other cell types combined together (Figure S9). CD31 cells showed significantly lower levels of PE(36:1), PE(38:3), and PS(38:3) than the other cell types. Two lysoPA species, (16:0p) and (18:1), and two major PS species containing polyunsaturated fatty acids (PUFA), (38:4) and (40:6), are elevated in macrophages (CD68). Further, GM3(24h:0) and PA(38:3) are elevated in B cells (CD20) and histone-labeled cells, respectively. Interestingly, the epithelial tumor (pan-cytokeratin) is associated with high levels of PI. Three PI species (40:6), (36:1), and (34:1) are among the top five species significantly elevated in cells expressing this marker. The proliferating cells (Ki-67) showed elevated levels of ganglioside GM3(24:0) and GM3(24:1). The pan-immune cells (CD45) exhibited low amounts of two cardiolipin species, CL(74:5) and CL(76:5).

We further compared the metabolome and lipidome of each of the cell types individually with each of the other cell types as shown in Table 1. NAPE(58:5p) along with CL(72:8) are the major lipids that differentiated the endothelial cells (CD31) from each of the other cell types. Similarly, PIs are the major lipids that distinguished epithelial tumor cells (pan-cytokeratin) from the rest. These results also confirmed the differential expression of some of the major PUFA-containing lipids such as PE(38:4), PI(40:6), and PS(38:4) among the different cell types.

Limitations and Outlook. This work presents the first attempt to successfully profile proteins, lipids, and metabolites on the same frozen-hydrated tissue at the single-cell level. GCIB-SIMS, especially using $(H_2O)_{n(n\geqslant 28k)}$-GCIB, has demonstrated its unique capability for the detection of a variety of lipids and metabolites in biological samples at unprecedented subcellular resolutions. Frozen-hydrated tissue preparation with cryogenic analysis preserved the integrity and compartmentalization of the pristine molecular constituents of cells, reflecting their abundance in specific cellular/subcellular compartments. The combination of $(H_2O)_n$-GCIB-SIMS performed on frozen-hydrated tissue with subsequent C_{60}-SIMS of lanthanide-tagged antibodies, effective in the identification of cell-specific markers, offers a unique opportunity to integrate valuable information related to proteins, lipids, and metabolites on the same sample and at the same level of high subcellular resolution. We are also aware of several limitations for this workflow. Current ToF mass spectrometer configurations are unable to differentiate isomeric species and have limited mass resolution ($m/\Delta m < 15,000$), which hinders differentiating isobaric species. This limits the untargeted profiling of multiple metabolites and lipids in the TME along with the discovery of diagnostic markers and new molecular targets. Moreover, although $(H_2O)_n$-GCIB produces less in-source fragmentation than

other GCIB-SIMS, there still is a noticeable amount which will interfere with ion assignments to endogenous species. However, other researchers have demonstrated that the fragmentation can be used for confident molecular annotations by matching the distribution patterns of the fragments and molecular species.[44] Ion assignments were performed using accurate mass matching and with assistance from literature references and our previous studies. Potential isomers and in-source fragmentation that normally occur with GCIB-SIMS have been noted within the study. Furthermore, the cell type identification in the TME is limited by the available selection of antibodies and stable lanthanide isotopes.

The goal of this study is to demonstrate a workflow that integrates lipidomic and metabolic profiling with spatial association to cell-specific proteins. We believe that our newly developed protocol combining two successive types of SIMS imaging opens up broad applications for exploring various biological phenomena of cell–cell interactions in normal physiology as well as in a wide variety of acute injuries and chronic disease conditions, including characterization of the TME in cancer biology. The optimization of the workflow and validation by other available techniques (e.g., other imaging mass spectrometries and immunofluorescence) will be incorporated in the future work.

■ ASSOCIATED CONTENT

ⓢ Supporting Information

The Supporting Information is available free of charge at https://pubs.acs.org/doi/10.1021/acs.analchem.0c05311.

> Materials and methods; lanthanide-tagged antibodies for IDC/DCIS and IDC tissue; selected ion species and empirical assignments from total negative ion mass spectrum; $(H_2O)_n$-GCIB-SIMS spectra and simulation spectra; time-of-flight (ToF) and beam spot size measurements; standard spectra of phosphatidylethanolamine PE 38:4, phosphatidylinositol PI 36:2, adenosine monophosphate (AMP), and adenosine triphosphate (ATP); aligned and overlaid $C_{60}/(H_2O)n$-GCIB SIMS images; $(H_2O)_n$-GCIB-SIMS images of IDC/DCIS and IDC tissue with the guidance of H&E staining; C_{60}-SIMS images of the same IDC/DCIS and IDC tissue post staining with lanthanide-tagged antibodies; OPLS-DA score plot of metabolites and lipids; and HCA dendrogram and OPLS-DA analysis on IDC tissue (PDF)

■ AUTHOR INFORMATION

Corresponding Author

Hua Tian — *Department of Chemistry, Pennsylvania State University, University Park, Pennsylvania 16802, United States;* ⓞ orcid.org/0000-0002-3598-0219; Email: hut3@psu.edu

Authors

Louis J. Sparvero — *Department of Environmental and Occupational Health and Center for Free Radical and Antioxidant Health, University of Pittsburgh, Pittsburgh, Pennsylvania 15261, United States; Children's Neuroscience Institute, UPMC Children's Hospital, University of Pittsburgh, Pittsburgh, Pennsylvania 15224, United States;* ⓞ orcid.org/0000-0001-6347-8448

Tamil Selvan Anthonymuthu − *Department of Environmental and Occupational Health and Center for Free Radical and Antioxidant Health, University of Pittsburgh, Pittsburgh, Pennsylvania 15261, United States; Department Critical Care Medicine, Safar Center for Resuscitation Research and Children's Neuroscience Institute, UPMC Children's Hospital, University of Pittsburgh, Pittsburgh, Pennsylvania 15224, United States;* ⓘ orcid.org/0000-0002-3460-5003

Wan-Yang Sun − *College of Pharmacy, Jinan University, Guangzhou, Guangdong 510632, P. R. China*

Andrew A. Amoscato − *Department of Environmental and Occupational Health and Center for Free Radical and Antioxidant Health, University of Pittsburgh, Pittsburgh, Pennsylvania 15261, United States; Children's Neuroscience Institute, UPMC Children's Hospital, University of Pittsburgh, Pittsburgh, Pennsylvania 15224, United States*

Rong-Rong He − *College of Pharmacy, Jinan University, Guangzhou, Guangdong 510632, P. R. China; School of Traditional Chinese Medicine, Jinan University, Guangzhou, Guangdong 510632, P. R. China*

Hülya Bayır − *Department of Environmental and Occupational Health and Center for Free Radical and Antioxidant Health, University of Pittsburgh, Pittsburgh, Pennsylvania 15261, United States; Department Critical Care Medicine, Safar Center for Resuscitation Research and Children's Neuroscience Institute, UPMC Children's Hospital, University of Pittsburgh, Pittsburgh, Pennsylvania 15224, United States;* ⓘ orcid.org/0000-0003-2361-4120

Valerian E. Kagan − *Department of Environmental and Occupational Health and Center for Free Radical and Antioxidant Health, University of Pittsburgh, Pittsburgh, Pennsylvania 15261, United States; Children's Neuroscience Institute, UPMC Children's Hospital, University of Pittsburgh, Pittsburgh, Pennsylvania 15224, United States; Departments of Chemistry, Radiation Oncology, Pharmacology and Chemical Biology, Chevron Science Center, University of Pittsburgh, Pittsburgh, Pennsylvania 15260, United States; Navigational Redox Lipidomics Group, Institute for Regenerative Medicine, IM Sechenov First Moscow State Medical University, Moscow 119435, Russia;* ⓘ orcid.org/0000-0002-7245-1885

Nicholas Winograd − *Department of Chemistry, Pennsylvania State University, University Park, Pennsylvania 16802, United States*

Complete contact information is available at:
https://pubs.acs.org/10.1021/acs.analchem.0c05311

Author Contributions

H.T. conceived the experiments, collected all the data, and compiled the first draft. L.J.S., T.S.A., and W.Y.S. performed the data processing for image alignment, HCA and OPLS-DA. H.B. and V.E.K. proposed the PCA data analysis. A.A.A., H.B., V.E.K., and R.R.H. discussed the significance and biological relevance of the results. H.T., L.J.S., A.A.A., H.B., and V.E.K. were the major contributors to writing and editing the text of the MS. N.W. edited the introduction. H.T., L.J.S., and T.S.A. contributed equally. All the authors participated in editing the paper.

Notes

The authors declare no competing financial interest.

■ REFERENCES

(1) Peng, A.; Mao, X.; Zhong, J.; Fan, S.; Hu, Y. *Proteomics* **2020**, *20*, 1900271.

(2) Hasin, Y.; Seldin, M.; Lusis, A. *Genome Biol.* **2017**, *18*, 83.

(3) Nam, A. S.; Chaligne, R.; Landau, D. A. *Nat. Rev. Genet.* **2021**, *22*, 3−18.

(4) Angerer, T. B.; Magnusson, Y.; Landberg, G.; Fletcher, J. S. *Anal. Chem.* **2016**, *88*, 11946−11954.

(5) Holzlechner, M.; Eugenin, E.; Prideaux, B. *Cancer Rep.* **2019**, *2*, No. e1229.

(6) Xu, G.; Li, J. *J. Comp. Neurol.* **2019**, *527*, 2158−2169.

(7) Zhang, J.; Sans, M.; Garza, K. Y.; Eberlin, L. S. *Mass Spectrom. Rev.* **2021**.

(8) Crecelius, A. C.; Schubert, U. S.; von Eggeling, F. *Analyst* **2015**, *140*, 5806−5820.

(9) Ifa, D. R.; Gumaelius, L. M.; Eberlin, L. S.; Manicke, N. E.; Cooks, R. G. *Analyst* **2007**, *132*, 461−467.

(10) Pasilis, S. P.; Kertesz, V.; Van Berkel, G. J.; Schulz, M.; Schorcht, S. *J. Mass Spectrom.* **2008**, *43*, 1627−1635.

(11) Griffiths, R. L.; Hughes, J. W.; Abbatiello, S. E.; Belford, M. W.; Styles, I. B.; Cooper, H. J. *J. Anal. Chem.* **2020**, *92*, 2885−2890.

(12) Bluestein, B. M.; Morrish, F.; Graham, D. J.; Guenthoer, J.; Hockenbery, D.; Porter, P. L.; Gamble, L. J. *Analyst* **2016**, *141*, 1947−1957.

(13) Fletcher, J. S.; Sämfors, S.; Vallin, J.; Svanström, A.; Grantham, J. *Anal. Bioanal. Chem.* **2021**, *413*, 445−453.

(14) Manzo, T.; Prentice, B. M.; Anderson, K. G.; Raman, A.; Schalck, A.; Codreanu, G. S.; Nava Lauson, C. B.; Tiberti, S.; Raimondi, A.; Jones, M. A.; Reyzer, M.; Bates, B. M.; Spraggins, J. M.; Patterson, N. H.; McLean, J. A.; Rai, K.; Tacchetti, C.; Tucci, S.; Wargo, J. A.; Rodighiero, S.; et al. *J. Exp. Med.* **2020**, *217*, No. e20191920.

(15) Ščupáková, K.; Dewez, F.; Walch, A. K.; Heeren, R. M. A.; Balluff, B. *Angew. Chem., Int. Ed.* **2020**, *59*, 17447−17450.

(16) Keren, L.; Bosse, M.; Marquez, D.; Angoshtari, R.; Jain, S.; Varma, S.; Yang, S.-R.; Kurian, A.; Van Valen, D.; West, R.; Bendall, S. C.; Angelo, M. *Cell* **2018**, *174*, 1373−1387.

(17) Jackson, H. W.; Fischer, J. R.; Zanotelli, V. R. T.; Ali, H. R.; Mechera, R.; Soysal, S. D.; Moch, H.; Muenst, S.; Varga, Z.; Weber, W. P.; Bodenmiller, B. *Nature* **2020**, *578*, 615−620.

(18) Lin, J.-R.; Izar, B.; Wang, S.; Yapp, C.; Mei, S.; Shah, P. M.; Santagata, S.; Sorger, P. K. *eLife* **2018**, *7*, No. e31657.

(19) Mistry, S.; Dakshinamoorthy, G.; Singh, J.; Nikulina, N.; Kim, J.; Bashier, R.; Gallina, M. E.; Kennedy-Darling, J. *J. Immunol.* **2019**, *202*, 130.23.

(20) Schürch, C. M.; Bhate, S. S.; Barlow, G. L.; Phillips, D. J.; Noti, L.; Zlobec, I.; Chu, P.; Black, S.; Demeter, J.; McIlwain, D. R.; Kinoshita, S.; Samusik, N.; Goltsev, Y.; Nolan, G. P. *Cell* **2020**, *183*, 838.

(21) Tian, H.; Sparvero, L. J.; Blenkinsopp, P.; Amoscato, A. A.; Watkins, S. C.; Bayır, H.; Kagan, V. E.; Winograd, N. *Angew. Chem., Int. Ed. Engl.* **2019**, *131*, 3188−3193.

(22) Fletcher, J. S.; Rabbani, S.; Henderson, A.; Blenkinsopp, P.; Thompson, S. P.; Lockyer, N. P.; Vickerman, J. C. *Anal. Chem.* **2008**, *80*, 9058−9064.

(23) McQuin, C.; Goodman, A.; Chernyshev, V.; Kamentsky, L.; Cimini, B. A.; Karhohs, K. W.; Doan, M.; Ding, L.; Rafelski, S. M.; Thirstrup, D.; Wiegraebe, W.; Singh, S.; Becker, T.; Caicedo, J. C.; Carpenter, A. E. *PLoS Biol.* **2018**, *16*, No. e2005970.

(24) Berrueta Razo, I.; Sheraz, S.; Henderson, A.; Lockyer, N. P.; Vickerman, J. C. *Rapid Commun. Mass Spectrom.* **2015**, *29*, 1851−1862.

(25) Sheraz, S.; Tian, H.; Vickerman, J. C.; Blenkinsopp, P.; Winograd, N.; Cumpson, P. *Anal. Chem.* **2019**, *91*, 9058−9068.

(26) Gandhi, N.; Das, G. *Cells* **2019**, *8*, 89.

(27) More, T. H.; RoyChoudhury, S.; Christie, J.; Taunk, K.; Mane, A.; Santra, M. K.; Chaudhury, K.; Rapole, S. *Oncotarget* **2017**, *9*, 2678−2696.

(28) Kapralov, A. A.; Yang, Q.; Dar, H. H.; Tyurina, Y. Y.; Anthonymuthu, T. S.; Kim, R.; St. Croix, C. M.; Mikulska-Ruminska, K.; Liu, B.; Shrivastava, I. H.; Tyurin, V. A.; Ting, H.-C.; Wu, Y. L.; Gao, Y.; Shurin, G. V.; Artyukhova, M. A.; Ponomareva, L. A.; Timashev, P. S.; Domingues, R. M.; Stoyanovsky, D. A.; et al. *Nat. Chem. Biol.* **2020**, *16*, 278−290.

(29) Stockwell, B. R.; Friedmann Angeli, J. P.; Bayir, H.; Bush, A. I.; Conrad, M.; Dixon, S. J.; Fulda, S.; Gascón, S.; Hatzios, S. K.; Kagan, V. E.; Noel, K.; Jiang, X.; Linkermann, A.; Murphy, M. E.; Overholtzer, M.; Oyagi, A.; Pagnussat, G. C.; Park, J.; Ran, Q.; Rosenfeld, C. S.; et al. *Cell* **2017**, *171*, 273−285.

(30) Gilligan, M. M.; Gartung, A.; Sulciner, M. L.; Norris, P. C.; Sukhatme, V. P.; Bielenberg, D. R.; Huang, S.; Kieran, M. W.; Serhan, C. N.; Panigrahy, D. *Proc. Natl. Acad. Sci. U.S.A.* **2019**, *116*, 6292−6297.

(31) Kang, S.; Han, J.; Song, S. Y.; Kim, W.-S.; Shin, S.; Kim, J. H.; Ahn, H.; Jeong, J.-H.; Hwang, S.-J.; Sung, J.-H. *Mol. Med. Rep.* **2015**, *12*, 5203−5210.

(32) Kim, D.; Li, H. Y.; Lee, J. H.; Oh, Y. S.; Jun, H.-S. *Exp. Mol. Med.* **2019**, *51*, 1−10.

(33) Cole, M. D.; Cowling, V. H. *Oncogene* **2009**, *28*, 1169−1175.

(34) Birklé, S.; Zeng, G.; Gao, L.; Yu, R. K.; Aubry, J. *Biochimie* **2003**, *85*, 455−463.

(35) Groux-Degroote, S.; Rodríguez-Walker, M.; Dewald, J. H.; Daniotti, J. L.; Delannoy, P. *Progress in Molecular Biology and Translational Science*; Schnaar, R. L., Lopez, P. H. H., Eds.; Academic Press, 2018; pp 197−227.

(36) Marquina, G.; Waki, H.; Fernandez, L. E.; Kon, K.; Carr, A.; Valiente, O.; Perez, R.; Ando, S. *Cancer Res.* **1996**, *56*, 5165−5171.

(37) Labrada, M.; Dorvignit, D.; Hevia, G.; Rodríguez-Zhurbenko, N.; Hernández, A. M.; Vázquez, A. M.; Fernández, L. E. *Semin. Oncol.* **2018**, *45*, 41−51.

(38) Chung, T.-W.; Choi, H.-J.; Park, M.-J.; Choi, H.-J.; Lee, S.-O.; Kim, K.-J.; Kim, C.-H.; Hong, C.; Kim, K.-H.; Joo, M.; Ha, K.-T. *Oncotarget* **2017**, *8*, 4436−4448.

(39) Dimri, M.; Bommi, P. V.; Sahasrabuddhe, A. A.; Khandekar, J. D.; Dimri, G. P. *Carcinogenesis* **2009**, *31*, 489−495.

(40) Abdelmagid, S. A.; MacKinnon, J. L.; Janssen, S. M.; Ma, D. W. L. *Nutr. Metab. Insights* **2016**, *9*, 71−84.

(41) Devanathan, N.; Jones, S.; Kaur, G.; Kimble-Hill, A. C. *Int. J. Mol. Sci.* **2020**, *21*, 2320.

(42) Gozzelino, L.; De Santis, M. C.; Gulluni, F.; Hirsch, E.; Martini, M. *Front. Oncol.* **2020**, *10*, 360.

(43) Segawa, K.; Nagata, S. *Trends Cell Biol.* **2015**, *25*, 639−650.

(44) Angerer, T. B.; Velickovic, D.; Nicora, C. D.; Kyle, J. E.; Graham, D. J.; Anderton, C.; Gamble, L. J. *Anal. Chem.* **2019**, *91*, 15073−15080.